Since January 2020 Elsevier has created a COVID-19 resource centre with free information in English and Mandarin on the novel coronavirus COVID-19. The COVID-19 resource centre is hosted on Elsevier Connect, the company's public news and information website.

Talanta 253 (2023) 124047

Contents lists available at ScienceDirect

Talanta

journal homepage: www.elsevier.com/locate/talanta

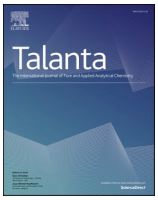

Photoacoustic detection of SARS-CoV-2 spike N501Y single-nucleotide polymorphism based on branched rolling circle amplification

Jiaying Xiao [a], Chuqi Yuan [a], Mingming Ding [a], Wei Hu [b], Zhengwen Hu [b], Bo Tian [a,*]

[a] Department of Biomedical Engineering, School of Basic Medical Science, Central South University, Changsha, Hunan, 410013, China
[b] Zybio Inc., No. 104 Cuibai Road, Chongqing, 400084, China

ARTICLE INFO

Keywords:
Photoacoustic biosensors
Rolling circle amplification
Single-nucleotide discrimination
SARS-CoV-2
N501Y

ABSTRACT

Rapid and accurate diagnosis of SARS-CoV-2 single-nucleotide variations is an urgent need for the initial detection of local circulation and monitoring the alternation of dominant variant. In this proof-of-concept study, a homogeneous and isothermal photoacoustic biosensor is demonstrated for rapid molecular amplification and detection of a synthetic DNA corresponding to SARS-CoV-2 spike N501Y. Branched rolling circle amplification produces single-stranded amplicons that can aggregate detection probe-modified AuNPs, which induces a strong photoacoustic signal at 640 nm due to both the surface plasmon resonance shift and the size-dependent effect of laser-induced nanobubbles, achieving a sub-femtomolar detection limit within a total assay time of 80 min. The limit of detection can be kept when measuring 5% serum samples. Moreover, the proposed biosensor is highly specific for single-nucleotide polymorphism discrimination and robust against background DNA.

1. Introduction

Omicron (B.1.1.529), the severe acute respiratory syndrome coronavirus 2 (SARS-CoV-2) variant of concern (VOC) designated at the end of 2021, exhibits multiple single-nucleotide mutations associated with enhanced cell entry, immune evasion, and infectivity, and has rapidly displaced Delta (B.1.617.2) in South Africa, Europe, and the USA as the most common SARS-CoV-2 variant [1–3]. Among these mutations, spike N501Y (i.e., A23063T) is a key mutation shared by Omicron and some other VOCs Alpha (B.1.1.7), Beta (B.1.351), and Gamma (P.1), which was reported to enhance the viral spike protein with improved affinity for cellular receptors but reduced affinity for neutralizing antibodies [4,5].

Nucleic acid point-of-care testing (POCT) can provide rapid and ease-of-use on-site bioanalysis in decentralized settings without specialized personnel, thus has been widely used in pathogen diagnosis [6,7]. The COVID-19 pandemic boosts the demand for timely and accurate diagnostics [8,9], resulting in an estimated compound annual growth rate of 10.8% for the size of POCT global market from 2022 to 2027 (marketsandmarkets.com; Report Code: MD 2702). As the standard nucleic acid detection method that is world-widely employed, qPCR (quantitative polymerase chain reaction) requires a sample pretreatment process to reduce both the matrix effects and the background noise (caused by, e.g., unbound fluorophores and light scattering) [10]. Moreover, discrimination of nucleotide variations by qPCR (and most of other POCT methodologies) relies on the sequence dependency of thermodynamics or kinetics [11,12], which exhibits a limited single-nucleotide resolution and is inferior to distinguish mixtures of wild type and mutant at different concentrations [13,14]. Therefore, robust sensing platforms in combination with molecular strategies capable of single-nucleotide discrimination are essential for timely control of Omicron as well as other possible VOCs coming up in the future.

The photoacoustic (PA) effect is the arising of sound waves caused by the optical absorption-induced thermal expansion of a material, which can be quantified by measuring the pressure changes through, e.g., microphones or piezoelectric sensors [15]. Owing to its capability of measuring light absorption of samples in various phases, this effect has been widely adopted in imaging and gas sensing [16–18]. Since the input and output are different kinds of energies, PA sensing can prevent the influences of reflected/scattered light, exhibiting a higher signal-to-noise ratio compared with other optical sensing strategies [19]. Therefore, PA sensing is promising for measuring biological sample matrix with none or minimal pretreatment, thus is desirable for in situ POCT [20,21]. For instance, Zhang et al. introduced a gas-microphone mode-based portable PA system for a series of

* Corresponding author.
E-mail address: tianbo@csu.edu.cn (B. Tian).

https://doi.org/10.1016/j.talanta.2022.124047
Received 30 March 2022; Received in revised form 11 October 2022; Accepted 22 October 2022
Available online 3 November 2022

enzymatic biochemical assays using chromogenic molecules as indicators [22–24].

Colloidal gold solutions can produce a remarkable strong PA signal: due to the localized surface plasmon resonance of gold nanoparticles (AuNPs), host liquid surrounding the laser-irradiated AuNP boils and generates a rapidly expanding vapor layer on the particle surface, thus producing an intense pressure change [25]. Zhao et al. demonstrated heterogeneous immunosensors for interleukin-8 and cryptococcal antigen, in which the target quantification was realized by measuring the presence of antibody-modified AuNPs, showing higher sensitivity compared with conventional colorimetric sensing [26,27]. Furthermore, the amplitude of nanobubble-induced PA signal strongly depends on the size of AuNPs [28], allowing for PA biosensing strategies based on analyte-induced aggregation of AuNP labels [29,30].

POCT of nucleic acid sequences containing single-nucleotide variations requires rapid and robust molecular amplification strategies capable of single-nucleotide discrimination. Among various isothermal amplification strategies, rolling circle amplification (RCA) has attracted significant attention due to its simplicity and robustness [31–34]. It was reported that 0.2% of blood could inhibit PCR completely [35,36], whereas RCA could be performed in 50% of blood [37]. Moreover, by employing a highly specific padlock probe (PLP) ligation process to prepare circular templates, RCA-based molecular detection strategies can distinguish single-nucleotide variants localized at the end of PLP [38,39], thus are promising for the molecular detection of SARS-CoV-2 VOCs. However, POCT applications of RCA are limited by its inferior amplification efficiency, which typically results in picomolar detection limits [40]. To address this issue, RCA-based strategies with improved efficiency have been developed, including circle-to-circle amplification [41,42], primer-generation RCA [43,44], nicking-enhanced RCA [45–47], etc. Branched RCA (BRCA) and hyperbranched RCA employed a secondary primer to hybridize with RCA amplicons for cascade or exponential amplification, producing single- or double-stranded final products through a branched DNA structure [48,49]. In this proof-of-concept study, we demonstrate a DNA biosensor based on PA effect, employing BRCA for the detection of a synthetic DNA sequence representing the Omicron N501Y variant. The final products of BRCA hybridized with detection probes grafted onto AuNPs, resulting in the aggregation of AuNPs and thus a strong PA signal induced by the optical absorption of a pulsed 640 nm laser. The proposed biosensor achieved rapid assay with a femtomolar detection limit and single-nucleotide resolution, which holds potential for POCT of SARS-CoV-2 VOCs.

2. Experimental section

2.1. Chemicals and DNA sequences

Gold(III) chloride hydrate (~50% Au basis), sodium citrate dihydrate (≥99%), thiol-PEG (MW 2000), salmon sperm DNA, and fetal bovine serum (FBS) were purchased from Sigma-Aldrich (St. Louis, MO, USA). Tris(2-carboxyethyl) phosphine (TCEP) was provided by Sangon Biotech (Shanghai, China) Co., Ltd. Ampligase and its working buffer were obtained from Lucigen (Middleton, MI, USA). Bst 3.0 polymerase, Bst buffer, and $MgSO_4$ were purchased from New England BioLabs (Ipswich, MA, USA). GL DNA Marker 5000 and dNTPs were prepared by Accurate Biotechnology (Hunan, China) Co., Ltd. Agarose was purchased from Biowest (Riverside, MO, USA). Phi29 polymerase, bovine serum albumin (BSA), SYBR Gold nucleic acid gel stain, Tris-HCl buffer (1 M, pH 8.0), and Tris-acetate-EDTA buffer (TAE, 50×) were provided by Thermo Fisher Scientific (Waltham, MA, USA). DNA sequences (listed in Table 1) including target (mutant and wild type), padlock probe (PLP), secondary primer (P_2), and detection probe (DP) were synthesized by Sangon Biotech and dissolved in Tris-HCl for storage. Unless otherwise specified, Tris-HCl (50 mM, pH 8.0) was employed as the buffer solution.

Table 1
DNA sequences used in this study. Position of the single-nucleotide polymorphism A23063T (corresponding to SARS-CoV-2 spike N501Y) is underlined.

Name	Sequence (5'→3')
Target (mutant)	TGG TTT CCA ACC CAC TTA TGG TGT TGG TTA CCA
Target (wild type)	TGG TTT CCA ACC CAC TAA TGG TGT TGG TTA CCA
Padlock probe (PLP)	Phosphate-AGT GGG TTG GAA ACC ATA TGA TAG AGC TAA TAT GAG ATA AAG CAG TGA CAT ACG ACA CGG TTG GTA ACC AAC ACC ATA
Secondary primer (P_2)	AAG CAG TGA CAT ACG ACA C
Detection probe (DP)	CTC ATA TTA GCT CTA TCA TAT GGT TTC CAA CCC TTT TTT TTT TTT TTT T-C3-Thiol

2.2. Preparation of AuNPs

AuNPs were prepared by the citrate reduction method and functionalized by thiol-probes based on the freezing-directed construction [50]. Briefly, $HAuCl_4$ aqueous solution was heated with stirring, followed by a quick injection of sodium citrate solution with a molecular ratio of 1:1.3. After 3 min, the color of the solution changed to wine red, and then the solution was cooled down to room temperature. Thiol-probes (10 μM, 10 μL) were reduced by TCEP (0.1 M) at room temperature for 30 min and mixed with the as-prepared AuNPs (39 nm, 0.8 nM, 100 μL). The mixture was frozen at −20°C for 2 h, followed by room temperature thawing. Thereafter, thiol-PEG (MW 2000, 2 mg/mL) was added to block the uncapped surface of AuNPs (incubated at 4°C for 48 h). Finally, DP-AuNPs were purified by 2 times of centrifugation (10 000 r/min, 10 min, LC-LX-H185C, Lichen Instrument Technology, Shaoxing, China) and resuspended to a particle concentration of 0.8 nM for storage at 4°C.

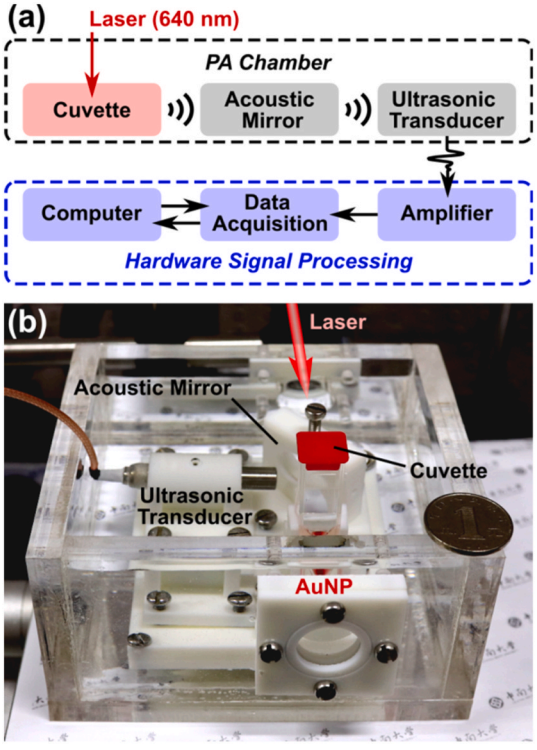

Fig. 1. PA apparatus. (a) Schematic of the electronic components for PA signal obtaining and processing. (b) Photograph of the water-filled PA chamber with a disposable cuvette, an acoustic mirror, and an ultrasonic transducer installed inside. The diameter of the coin used for scale is 25 mm.

2.3. PA apparatus

As illustrated in Fig. 1a, the PA detection system consists of (1) an optical parametric oscillator (SpitLight OPO 600 mid-band, InnoLas, Krailling, Germany) generating a 640 nm pulsed laser (24 mJ, 20 Hz), (2) a PA chamber filled with deionized water, (3) a pulser/receiver (DPR500, Imaginant, Pittsford, NY, USA) used as an amplifier (55 dB gain for signals in the range of 2.5–10 MHz), and (4) a data-acquisition device (NI PCI-5124, 200 MS/s, 12-Bit, National Instruments Corporation, Austin, TX, USA) in the computer. The acrylic PA chamber (see Fig. 1b) was designed with two glass windows (for the laser to pass through) and several 3D printed sample modules (made of ABS resin) to position (2.1) a Sarstedt disposable cuvette (REF 67.758.001, Nümbrecht, Germany), (2.2) an acoustic mirror, and (2.3) a water-immersion ultrasonic transducer (5 MHz center frequency, Shanghai Zunen Nondestructive Testing Technology, Shanghai, China). A LabVIEW interface is used to drive the laser and record the signal at the ultrasonic transducer. For PA measurements, the laser passed right through the underwater part of the cuvette containing the AuNP suspension, generating a PA signal that was transmitted to the ultrasonic transducer by the acoustic mirror. To compensate for the system errors caused by, e.g., electrostatic interference and position changes, the output PA signal was normalized by that of a control sample (containing 0.1 nM of AuNPs or DP-AuNPs) measured in each experiment.

2.4. Characterization of AuNP aggregates

To investigate the influences of AuNP assembly on PA signal, absorption spectra of dispersed/aggregated AuNPs were obtained (N4S UV-VIS spectrophotometer, INESA Analytical Instrument, Shanghai, China). Hydrodynamic size changes of AuNPs were characterized by dynamic light scattering (DLS) with BeNano 90 particle size analyzer (Bettersize Instruments, Dandong, China) equipped with a 671 nm laser and operating at an angle of 90° at 25°C.

2.5. Padlock probe ligation, BRCA, and PA measurement

Padlock probe ligation was conducted at 50°C for 15 min in a reaction mixture containing Ampligase (0.25 U/μL), ligation buffer (1×), PLP (60 nM), target DNA (20 nM), and BSA (0.2 μg/μL). Thereafter, the mixture (20 nM) was diluted to desired concentrations for BRCA. In the amplification process, a reaction mixture of 60 μL was prepared by mixing the ligation mixture (15 μL), P_2 (10 μM, 6 μL), DP-AuNPs (0.8 nM, 15 μL), $MgSO_4$ (100 mM, 3.6 μL), dNTPs (10 mM, 2 μL), Bst buffer (10×, 6 μL), Bst 3.0 polymerase (8 U/μL, 2 μL), and H_2O (10.4 μL). The BRCA suspension was incubated at 60°C for 1 h. Thereafter, the suspension was diluted with 60 μL of H_2O (the final concentration of AuNP was 0.1 nM) and pipetted to the cuvette for PA measurement.

2.6. Gel electrophoresis

Agarose gel electrophoresis (2.5%, 1×TAE) was performed to demonstrate the ligation and amplification. Samples to be analyzed were mixed with SYBR Gold and loading buffer, followed by electrophoresis at room temperature (100 V, 45 min) and image taken (OI 100 gel imaging system, Guangzhou BIO-OI Biotechnology, Guangzhou, China).

3. Results and discussion

3.1. Sensing principle

Based on the SARS-CoV-2 sequences shared in GISAID (www.gisaid.org), a 33-nt-long single-stranded DNA sequence containing single-nucleotide polymorphism A23063T (corresponding to SARS-CoV-2 spike N501Y) was synthesized as the target sequence (Table 1). For target quantification (illustrated in Fig. 2, blue arrows), the assay is initiated with a target-mediated PLP ligation process to prepare circular templates. As a proof-of-concept, the targets hybridized with the circular templates act as primers to initiate the polymerase reaction. In practice, primer-hybridized PLP would be used in the ligation process to obtain circular templates with attached primers. As a cascade amplification strategy, BRCA consists of two amplification reactions that are performed simultaneously and homogeneously: a conventional RCA reaction produces long single-stranded intermediate amplicons, which can be recognized by P_2 (as well as remaining unligated PLP) for the secondary amplification (i.e., stand-displacement amplification), generating single-stranded end amplicons. End amplicons of BRCA can hybridize with DPs grafted onto AuNPs, leading to AuNP aggregation. The reaction suspension (containing AuNPs) is detected photoacousticly in the cuvette positioned in the PA chamber. Since Ampligase conducts highly stringent ligation, the mismatch between wild type sequence (i.e., a reference sequence without A23063T, from GenBank NC_045512.2) and PLP hinders the ligation, avoiding the following BRCA (gray arrows in Fig. 2). Either DNA or RNA targets can be used for the preparation of circular templates under an identical reaction principle.

3.2. Sensing the size-dependent PA effect of AuNPs

Delocalized conduction electrons shared among aggregated AuNPs could result in a redshift of surface plasmon resonance (SPR) response [51,52]. Accordingly, aggregation of AuNPs influences the PA signal due to the changes of optical absorption at certain wavelengths. Moreover, the effect of laser-induced nanobubbles (LINB) strongly depends on the size of AuNPs, causing a dramatic aggregation-induced PA signal increase independent from the optical absorption changes [28]. However, by evaluating AuNPs with diameters ranging from 12.5 to 83.3 nm, González et al. found that large AuNPs generate nanobubbles of largely distributed sizes (leading to interference and signal broadening), and the best PA sensing performances were obtained when using AuNPs around 20–40 nm [28,29]. Considering that we employed the same AuNP preparation method (that led to similar particle size distributions, characterized by DLS), we decided to follow their conclusion and chose 37 nm sized AuNPs for this study to balance the strength and precision of the PA response.

PA volumetric sensing measures an ensemble average PA signal coming from the entire measured volume, suggesting a limited sensing resolution due to the dominance of unbound AuNPs (generating a high level of background signal) especially when measuring weak positive samples. Therefore, we first determined the working concentration of AuNP to balance the detection sensitivity with the robustness against system disturbance. The PA amplitudes of AuNPs at concentrations ranging from 10 pM to 0.8 nM were obtained using 521 nm and 640 nm lasers (Fig. S1), which shows that the PA amplitude varies linearly with the AuNP concentration, and that the setup achieved desirable signal-to-noise ratios at AuNP concentrations down to 0.1 nM. Hence, a working concentration of 0.1 nM AuNPs was chosen for the following experiments.

To explore the PA response of AuNP aggregates (under a 640 nm laser), gradually aggregated AuNPs were prepared by adding $MgSO_4$ of different concentrations to 0.1 nM of naked AuNPs. As shown in Fig. 3a, UV–vis absorption spectra of gradually aggregated AuNPs (induced by 0.1–0.7 mM $MgSO_4$) can be characterized by the decrease of absorption at 521 nm as well as a correspondingly increase of broad absorption at longer wavelengths. In addition to the changes of optical absorption, the hydrodynamic size changes of AuNPs aggregated by 0.1–0.8 mM $MgSO_4$ were confirmed by the DLS measurement (Fig. 3b), showing gradual increases from 37 to 136 nm. Micron-sized aggregates were also found but located out of the reliable detection range of DLS and not shown. The PA spectra (Fig. 3c, irradiated by a 640 nm laser) of the gradually aggregated AuNPs normalized by the amplitude of 0.1 nM naked AuNPs, which were recorded after 20.25 μs (compensating the ca. 30 mm

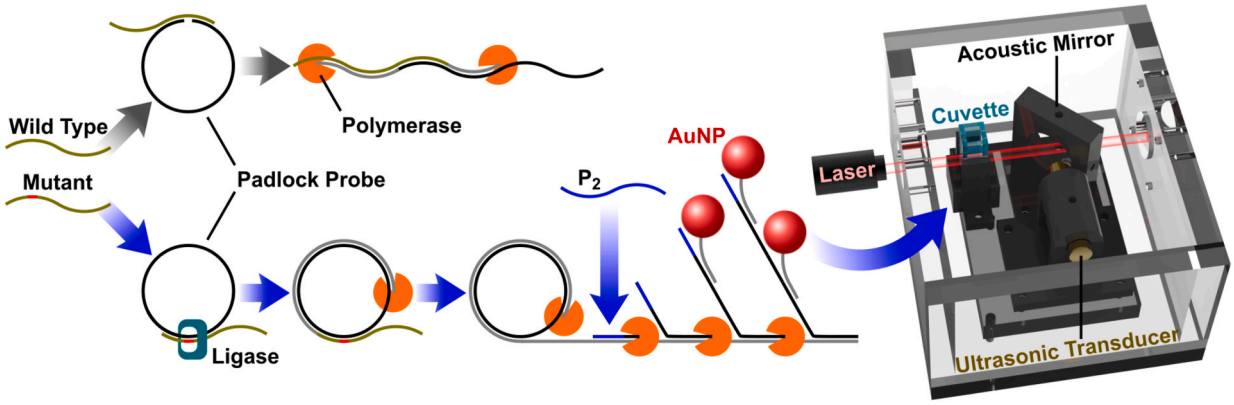

Fig. 2. Schematic illustration of BRCA and PA chamber. Target mutant sequences are ligated and then amplified, generating single-stranded end amplicons that can aggregate AuNPs for the following PA measurement. All the reaction processes can be performed homogeneously and the reaction can be measured volumetrically.

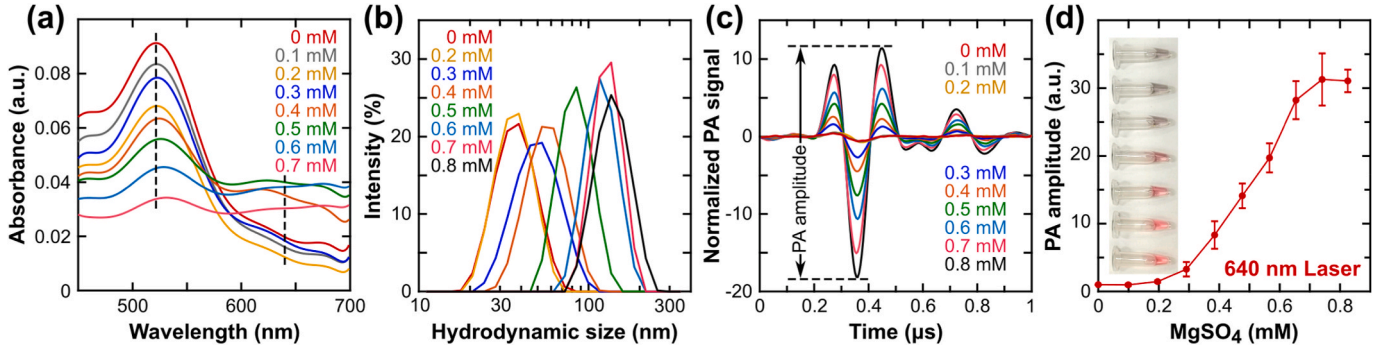

Fig. 3. Feasibility tests of PA quantification by comparing (a) UV–vis absorption spectra, (b) DLS-based size distributions, and (c) representative PA spectra (irradiated by a 640 nm laser) of $MgSO_4$-induced gradually aggregated AuNPs, normalized by the amplitude of 0.1 nM naked AuNPs. The black dashed lines in (a) indicate the positions of 521 and 640 nm. (d) The dose-response curve of maximum normalized PA signal difference vs. $MgSO_4$ concentration. Error bars indicate the standard deviations of five independent replicates. The inset in (d) shows a photograph of 4 times concentrated gradually aggregated AuNPs.

distance from the cuvette to the ultrasonic transducer). Notably, PA spectra show that the strongest ultrasonic waves were obtained within 0.2–0.5 μs, suggesting that a sample thickness of 0.45 mm (corresponding to 0.3 μs of ultrasonic wave transmission in water) could be enough for PA quantification and thus the feasibility of microfluidic PA devices in the future. The maximum differences in normalized PA signal (between the maximum negative amplitude and the maximum positive amplitude) were recorded as the PA amplitude and plotted against the concentration of $MgSO_4$ (Fig. 3d), showing a dynamic response range of 0.2–0.7 mM $MgSO_4$. Four times concentrated AuNPs (0.4 nM) were prepared and aggregated (Fig. 3d inset) by different concentrations of $MgSO_4$ (0, 0.8, 1.2, 1.6, 2.0, 2.4, 2.8 mM), indicating that a PA amplitude of ca. 3 a.u. is corresponding to an observable AuNP aggregation.

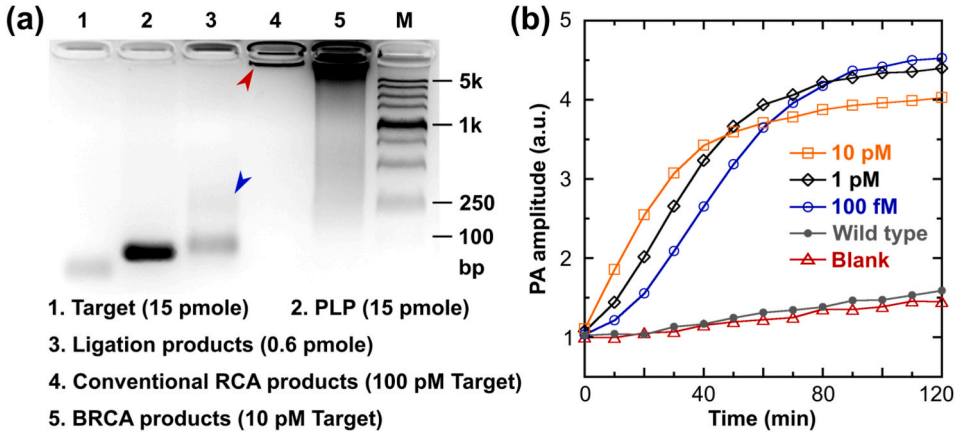

Fig. 4. Feasibility test for BRCA. (a) Agarose gel electrophoresis analysis of target (lane 1), PLP (lane 2), ligation products (lane 3), conventional RCA products (lane 4), and BRCA products (lane 5). (b) Time-resolved changes of PA amplitude for the proposed biosensing strategy (irradiated by a 640 nm laser and normalized by the initial PA amplitude of blank control at 0 min).

3.3. BRCA feasibility test

To demonstrate the molecular reaction as well as the probe design, gel electrophoresis analysis was applied to evaluate products of the ligation process, conventional RCA, and BRCA (see Fig. 4a). Compared to the target band (lane 1) and PLP band (lane 2), the slower band in lane 3 indicates loop structures formed by target-PLP hybridization. During the ligation reaction, larger loop or linear structures containing several PLPs and targets can be formed, generating a smear following the band (indicated by a blue arrow). The synthesized target DNA containing single-nucleotide polymorphism A23063T was probed by PLP followed by Bst 3.0 polymerase-based conventional RCA (lane 4) or BRCA (lane 5). For conventional RCA, 100 pM of target DNA was amplified without adding P_2, forming a heavy band corresponding to the long single-stranded DNA products (indicated by a red arrow). For BRCA of 10 pM target sequence, P_2 hybridized with the long single-stranded RCA amplicons and triggered the cascade amplification, generating end amplicons of various lengths. The thick and heavy band of BRCA amplicon, as well as the short products, suggested a higher amplification efficiency compared to conventional RCA. Note that sequences and most amplicons are single-stranded, and thus cannot be simply compared with the marker in lane M. For comparison, phi29 polymerase-based RCA and BRCA were analyzed as well (Fig. S2). Due to the exonuclease activity of phi29, both P_2 and amplicons were digested during the reaction, resulting in fewer products that could hardly induce detectable AuNP aggregation. Therefore, Bst 3.0 was chosen in this study.

We next performed BRCA with DP-AuNPs and compared the time-resolved PA outputs of three positive samples containing 100 fM, 1 pM, and 10 pM target DNA (mutant), respectively. A blank control sample (buffer solution) and a negative control sample (1 pM of wild type target) were analyzed as well. As shown in Fig. 4b, BRCA with higher target concentrations expressed sharper curve slopes and tended to be stable earlier. The PA signal remained increasing after the rapid increase stage, which can be ascribed to the nonspecific aggregation of AuNP triggered by the reaction temperature (60°C) and laser-induced local heating. Compared to the low concentration samples, the sample containing the highest target concentration (10 pM) reached the lowest PA signal plateau. The hook effect was caused by the large amount of rapidly produced short amplicons, which saturated all DPs grafted onto AuNPs and avoided the formation of AuNP aggregates. As a result, a negative correlation between the PA plateau values and target concentrations can be observed.

3.4. BRCA-based target quantification

DNA quantification study was performed using the synthetic A23063T target. After PLP probing and BRCA, target-induced AuNP aggregation was detected by the proposed PA biosensor. Despite the clearly observable color changes, BRCA-induced AuNP aggregations have noisier PA spectra with smaller amplitudes (Fig. 5a) compared to the $MgSO_4$-induced AuNP aggregates (Fig. 3c). It can be explained by the DNA coils among AuNPs and the deposition of MgPPi, both of which influenced the delocalization of conduction electrons and thus the SPR. End-point PA responses obtained after 60 min of BRCA were recorded for the dose-response curve (Fig. 5b). Herein, the PA response is defined as the normalized increase of PA amplitude, $(S - S_0)/(B - B_0)$, where S_0 and S represent the PA amplitudes of the sample before and after BRCA reaction, respectively, while B_0 and B represent the PA amplitudes of the blank control before and after BRCA reaction, respectively. The PA response had a monotonic positive correlation with the target concentration between 0.1 fM and 1 pM, with a dynamic detection range of ca. 3 orders of magnitude. A cutoff line was plotted as the average signal plus three standard deviations (σ) of the blank controls. Based on the 3σ criterion, a limit of detection (LOD) of 0.3 fM was achieved by the proposed method. The average coefficient of variation in the dynamic detection range of 1–1000 fM was 7.5%, suggesting good repeatability. Compared to other RCA-based amplification methods capable of single-nucleotide discrimination (Table S1), the proposed strategy shows an improved LOD due to the LINB effect (which can be regarded as one additional signal amplification process).

3.5. Target quantification in serum

Considering that the applicability of both AuNPs and RCA were fully demonstrated using simulated biological samples and real samples by other groups [21,53,54], we expect that the PA biosensor holds potential in analyzing complex samples. To investigate the influences of matrix effects, series dilutions of targets were prepared in buffer solution containing 5% FBS for BRCA and PA analysis. Due to increased nonspecific binding, the PA responses found in FBS samples were lower than those obtained in pure buffer for the same target concentration (cf. Figs. S3 and 5b), resulting in decreased sensitivity but a similar LOD of 0.5 fM. Considering that the 20-fold diluted serum still contains a higher concentration of background biomacromolecules (and thus stronger matrix effects) than nasopharyngeal swab samples commonly used in SARS-CoV-2 diagnostics, this test proves the robustness of the proposed method in analyzing biological samples.

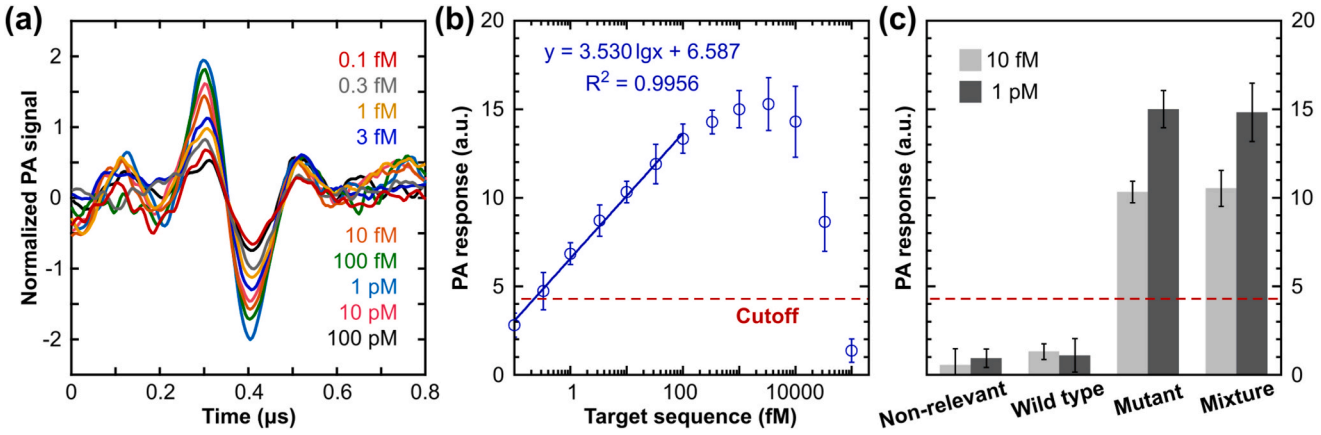

Fig. 5. BRCA-based PA quantification of synthetic SARS-CoV-2 spike N501Y DNA. (a) Representative PA spectra (under 640 nm irradiation) of different target concentrations after 60 min of BRCA, normalized by the blank control sample. (b) Dose-response curve of target detection based on the proposed PA biosensor. (c) Specificity test. PA responses after 60 min of BRCA for 10 fM and 1 pM of indicated sequences. The red dashed lines indicate the cutoff value. Error bars indicate the standard deviations of five independent replicates. (For interpretation of the references to color in this figure legend, the reader is referred to the Web version of this article.)

3.6. Specificity test

The PLP ligation-based RCA strategy can discriminate single-nucleotide polymorphism and therefore holds the potential to distinguish SARS-CoV-2 VOCs, which is of high importance in COVID-19 control. Non-relevant DNA (sheared salmon sperm DNA with an average size of 150 nt) and synthetic wild type sequence were detected at 10 fM and 1 pM using the proposed method and compared with the results of target (mutant) sequence (see Fig. 5c). Mixtures of all three kinds of sequences were also tested. After PLP ligation and BRCA, end-point PA responses of both wild type sequence and non-relevant DNA were measured, which were close to the average value of blank controls used for normalization. Moreover, mixtures containing all three kinds of sequences gave similar PA responses to these obtained from samples containing target only, indicating both the specificity and the robustness (against background amplification) of the proposed PA biosensor.

4. Conclusions

In summary, a homogeneous and isothermal PA biosensor was demonstrated for molecular amplification and detection of a synthetic DNA representing SARS-CoV-2 spike N501Y. BRCA amplicons aggregated DP-AuNPs and induced a strong PA signal at 640 nm due to the SPR shift as well as the size-dependent LINB effect, achieving a sub-femtomolar LOD. Thereafter, we evaluated the specificity of the proposed biosensor for single-nucleotide polymorphism discrimination and its robustness against background amplification, demonstrating its potential applicability to rapid detection and control of SARS-CoV-2 variants of concern.

Credit authorship statement

Jiaying Xiao: Conceptualization, Methodology, Writing – review & editing, Supervision. Chuqi Yuan: Methodology, Formal analysis, Investigation, Visualization. Mingming Ding: Methodology, Validation, Investigation. Wei Hu: Resources, Writing – review & editing. Zhengwen Hu: Resources, Formal analysis. Bo Tian: Conceptualization, Visualization, Writing – original draft, Project administration.

Declaration of competing interest

The authors declare that they have no known competing financial interests or personal relationships that could have appeared to influence the work reported in this paper.

Data availability

Data will be made available on request.

Acknowledgements

This work was financially supported by the National Natural Science Foundation of China (No. 32101214), the Hunan Provincial Natural Science Foundation of China (No. 2022JJ40582), and the Fundamental Research Funds for the Central Universities of Central South University (No. 202045006).

Appendix A. Supplementary data

Supplementary data to this article can be found online at https://doi.org/10.1016/j.talanta.2022.124047.

References

[1] S.S.A. Karim, Q.A. Karim, Omicron SARS-CoV-2 variant: a new chapter in the COVID-19 pandemic, Lancet 398 (2021) 2126–2128, https://doi.org/10.1016/s0140-6736(21)02758-6.
[2] C. Del Rio, S.B. Omer, P.N. Malani, Winter of omicron—the evolving COVID-19 pandemic, JAMA 327 (2021) 319–320, https://doi.org/10.1136/bmj.n3104.
[3] D.P. Martin, S. Weaver, H. Tegally, J.E. San, S.D. Shank, E. Wilkinson, A.G. Lucaci, J. Giandhari, S. Naidoo, Y. Pillay, L. Singh, R.J. Lessells, R.K. Gupta, J. O. Wertheim, A. Nekturenko, B. Murrell, G.W. Harkins, P. Lemey, O.A. MacLean, D. L. Robertson, T. de Oliveira, S.L. Kosakovsky Pond, The emergence and ongoing convergent evolution of the SARS-CoV-2 N501Y lineages, Cell 184 (2021) 5189–5200, https://doi.org/10.1016/j.cell.2021.09.003.
[4] F. Tian, B. Tong, L. Sun, S. Shi, B. Zheng, Z. Wang, X. Dong, P. Zheng, N501Y mutation of spike protein in SARS-CoV-2 strengthens its binding to receptor ACE2, Elife 10 (2021), e69091, https://doi.org/10.7554/eLife.69091.
[5] Y. Liu, J. Liu, K.S. Plante, J.A. Plante, X. Xie, X. Zhang, Z. Ku, Z. An, D. Scharton, C. Schindewolf, S.G. Widen, V.D. Menachery, P.-Y. Shi, S.C. Weaver, The N501Y spike substitution enhances SARS-CoV-2 infection and transmission, Nature 602 (2021) 294–299, https://doi.org/10.1038/s41586-021-04245-0.
[6] V. Gubala, L.F. Harris, A.J. Ricco, M.X. Tan, D.E. Williams, Point of care diagnostics: status and future, Anal. Chem. 84 (2012) 487–515, https://doi.org/10.1021/ac2030199.
[7] M. Zarei, Advances in point-of-care technologies for molecular diagnostics, Biosens. Bioelectron. 98 (2017) 494–506, https://doi.org/10.1016/j.bios.2017.07.024.
[8] B. Hengel, L. Causer, S. Matthews, K. Smith, K. Andrewartha, S. Badman, B. Spaeth, A. Tangey, P. Cunningham, A. Saha, E. Phillips, J. Ward, C. Watts, J. King, T. Applegate, M. Shephard, R. Guy, A decentralised point-of-care testing model to address inequities in the COVID-19 response, Lancet Infect. Dis. 21 (2021) e183–e190, https://doi.org/10.1016/S1473-3099(20)30859-8.
[9] Q. Song, X. Sun, Z. Dai, Y. Gao, X. Gong, B. Zhou, J. Wu, W. Wen, Point-of-care testing detection methods for COVID-19, Lab Chip 21 (2021) 1634–1660, https://doi.org/10.1039/d0lc01156h.
[10] V.M. Corman, O. Landt, M. Kaiser, R. Molenkamp, A. Meijer, D.K.W. Chu, T. Bleicker, S. Brünink, J. Schneider, M.L. Schmidt, D.G.J.C. Mulders, B. L. Haagmans, B. Van Der Veer, S. Van Den Brink, L. Wijsman, G. Goderski, J. L. Romette, J. Ellis, M. Zambon, M. Peiris, H. Goossens, C. Reusken, M.P. G. Koopmans, C. Drosten, Detection of 2019 novel coronavirus (2019-nCoV) by real-time RT-PCR, Euro Surveill. 25 (2020), 2000045, https://doi.org/10.2807/1560-7917.ES.2020.25.3.2000045.
[11] S.X. Chen, G. Seelig, An engineered kinetic amplification mechanism for single nucleotide variant discrimination by DNA hybridization probes, J. Am. Chem. Soc. 138 (2016) 5076–5086, https://doi.org/10.1021/jacs.6b00277.
[12] D.Y. Zhang, S.X. Chen, P. Yin, Optimizing the specificity of nucleic acid hybridization, Nat. Chem. 4 (2012) 208–214, https://doi.org/10.1038/nchem.1246.
[13] A. Abi, A. Safavi, Targeted detection of single-nucleotide variations: progress and promise, ACS Sens. 4 (2019) 792–807, https://doi.org/10.1021/acssensors.8b01604.
[14] N. Li, Y. Zhao, Y. Liu, Z. Yin, R. Liu, L. Zhang, L. Ma, X. Dai, D. Zhou, X. Su, Self-resetting molecular probes for nucleic acids detection enabled by fuel dissipative systems, Nano Today 41 (2021), 101308, https://doi.org/10.1016/j.nantod.2021.101308.
[15] A.G. Bell, On the production and reproduction of sound by light, Am. J. Sci. s3–20 (1880) 305–324, https://doi.org/10.2475/ajs.s3-20.118.305.
[16] L.V. Wang, S. Hu, Photoacoustic tomography: in vivo imaging from organelles to organs, Science 335 (2012) 1458–1462, https://doi.org/10.1126/science.1216210.
[17] J. Du, S. Yang, Y. Qiao, H. Lu, H. Dong, Recent progress in near-infrared photoacoustic imaging, Biosens. Bioelectron. 191 (2021), 113478, https://doi.org/10.1016/j.bios.2021.113478.
[18] S. Palzer, Photoacoustic-based gas sensing: a review, Sensors 20 (2020) 2745, https://doi.org/10.3390/s20092745.
[19] R.B. Somoano, Photoacoustic spectroscopy of condensed matter, Angew. Chem. Int. Ed. 17 (1978) 238–245, https://doi.org/10.1002/anie.197802381.
[20] A.S. Jeevarathinam, N. Pai, K. Huang, A. Hariri, J. Wang, Y. Bai, L. Wang, T. Hancock, S. Keys, W. Penny, J.V. Jokerst, A cellulose-based photoacoustic sensor to measure heparin concentration and activity in human blood samples, Biosens. Bioelectron. 126 (2019) 831–837, https://doi.org/10.1016/j.bios.2018.11.052.
[21] W. Cao, W. Gao, Z. Liu, W. Hao, X. Li, Y. Sun, L. Tong, B. Tang, Visualizing miR-155 to monitor breast tumorigenesis and response to chemotherapeutic drugs by a self-assembled photoacoustic nanoprobe, Anal. Chem. 90 (2018) 9125–9131, https://doi.org/10.1021/acs.analchem.8b01537.
[22] Y.J. Zhang, S. Chen, Y.L. Yu, J.H. Wang, A miniaturized photoacoustic device with laptop readout for point-of-care testing of blood glucose, Talanta 209 (2020), 120527, https://doi.org/10.1016/j.talanta.2019.120527.
[23] Y.J. Zhang, L. Guo, S. Chen, Y.L. Yu, J.H. Wang, A portable photoacoustic device for facile and sensitive detection of serum alkaline phosphatase activity, Anal. Chim. Acta 1108 (2020) 54–60, https://doi.org/10.1016/j.aca.2020.02.054.
[24] Y.J. Zhang, L. Guo, Y.L. Yu, J.H. Wang, Photoacoustic-based miniature device with smartphone readout for point-of-care testing of uric acid, Anal. Chem. 92 (2020) 15699–15704, https://doi.org/10.1021/acs.analchem.0c03470.
[25] S. Egerev, S. Ermilov, O. Ovchinnikov, A. Fokin, D. Guzatov, V. Klimov, A. Kanavin, A. Oraevsky, Acoustic signals generated by laser-irradiated metal

nanoparticles, Appl. Opt. 48 (2009) C38–C45, https://doi.org/10.1364/AO.48.000C38.
[26] Y. Zhao, M. Cao, J.F. McClelland, Z. Shao, M. Lu, A photoacoustic immunoassay for biomarker detection, Biosens. Bioelectron. 85 (2016) 261–266, https://doi.org/10.1016/j.bios.2016.05.028.
[27] Y. Zhao, Y. Huang, X. Zhao, J.F. McClelland, M. Lu, Nanoparticle-based photoacoustic analysis for highly sensitive lateral flow assays, Nanoscale 8 (2016) 19204–19210, https://doi.org/10.1039/c6nr05312b.
[28] M.G. González, X. Liu, R. Niessner, C. Haisch, Strong size-dependent photoacoustic effect on gold nanoparticles by laser-induced nanobubbles, Appl. Phys. Lett. 96 (2010), 174104, https://doi.org/10.1063/1.3387890.
[29] X. Liu, M.G. González, R. Niessner, C. Haisch, Strong size-dependent photoacoustic effect on gold nanoparticles: a sensitive tool for aggregation-based colorimetric protein detection, Anal. Methods 4 (2012) 309–311, https://doi.org/10.1039/c1ay05497j.
[30] Z. Yasmin, E. Khachatryan, Y.H. Lee, S. Maswadi, R. Glickman, K.L. Nash, Vitro monitoring of oxidative processes with self-aggregating gold nanoparticles using all-optical photoacoustic spectroscopy, Biosens. Bioelectron. 64 (2015) 676–682, https://doi.org/10.1016/j.bios.2014.09.078.
[31] M.M. Ali, F. Li, Z. Zhang, K. Zhang, D.K. Kang, J.A. Ankrum, X.C. Le, W. Zhao, Rolling circle amplification: a versatile tool for chemical biology, materials science and medicine, Chem. Soc. Rev. 43 (2014) 3324–3341, https://doi.org/10.1039/c3cs60439j.
[32] R.R.G. Soares, N. Madaboosi, M. Nilsson, Rolling circle amplification in integrated microsystems: an uncut gem toward massively multiplexed pathogen diagnostics and genotyping, Acc. Chem. Res. 54 (2021) 3979–3990, https://doi.org/10.1021/acs.accounts.1c00438.
[33] H.X. Jiang, Z.Z. Liang, Y.H. Ma, D.M. Kong, Z.Y. Hong, G-quadruplex fluorescent probe-mediated real-time rolling circle amplification strategy for highly sensitive microRNA detection, Anal. Chim. Acta 943 (2016) 114–122, https://doi.org/10.1016/j.aca.2016.09.019.
[34] H.X. Jiang, M.Y. Zhao, C. Di Niu, D.M. Kong, Real-time monitoring of rolling circle amplification using aggregation-induced emission: applications in biological detection, Chem. Commun. 51 (2015) 16518–16521, https://doi.org/10.1039/c5cc07340e.
[35] W. Abu Al-Soud, P. Rådström, Effects of amplification facilitators on diagnostic PCR in the presence of blood, feces, and meat, J. Clin. Microbiol. 38 (2000) 4463–4470, https://doi.org/10.1128/jcm.38.12.4463-4470.2000.
[36] C. Schrader, A. Schielke, L. Ellerbroek, R. Johne, PCR inhibitors - occurrence, properties and removal, J. Appl. Microbiol. 113 (2012) 1014–1026, https://doi.org/10.1111/j.1365-2672.2012.05384.x.
[37] M. Liu, Q. Zhang, Z. Li, J. Gu, J.D. Brennan, Y. Li, Programming a topologically constrained DNA nanostructure into a sensor, Nat. Commun. 7 (2016) 1–7, https://doi.org/10.1038/ncomms12074.
[38] M. Nilsson, H. Malmgren, M. Samiotaki, M. Kwiatkowski, B.P. Chowdhary, U. Landegren, Padlock probes: circularizing oligonucleotides for localized DNA detection, Science 265 (1994) 2085–2088, https://doi.org/10.1126/science.7522346.
[39] M. Nilsson, G. Barbany, D.O. Antson, K. Gertow, U. Landegren, Enhanced detection and distinction of RNA by enzymatic probe ligation, Nat. Biotechnol. 18 (2000) 791–793, https://doi.org/10.1038/77367.
[40] Z. Huang, J. Li, H. Zhong, B. Tian, Nucleic acid amplification strategies for volume-amplified magnetic nanoparticle detection assay, Front. Bioeng. Biotechnol. 10 (2022), 939807, https://doi.org/10.3389/fbioe.2022.939807.
[41] F. Dahl, J. Banér, M. Gullberg, M. Mendel-Hartvig, U. Landegren, M. Nilsson, Circle-to-circle amplification for precise and sensitive DNA analysis, Proc. Natl. Acad. Sci. USA 101 (2004) 4548–4553, https://doi.org/10.1073/pnas.0400834101.
[42] B. Tian, F. Gao, J. Fock, M. Dufva, M.F. Hansen, Homogeneous circle-to-circle amplification for real-time optomagnetic detection of SARS-CoV-2 RdRp coding sequence, Biosens. Bioelectron. 165 (2020), 112356, https://doi.org/10.1016/j.bios.2020.112356.
[43] T. Murakami, J. Sumaoka, M. Komiyama, Sensitive isothermal detection of nucleic-acid sequence by primer generation-rolling circle amplification, Nucleic Acids Res. 37 (2009) e19, https://doi.org/10.1093/nar/gkn1014.
[44] B. Tian, G.A.S. Minero, J. Fock, M. Dufva, M.F. Hansen, CRISPR-Cas12a based internal negative control for nonspecific products of exponential rolling circle amplification, Nucleic Acids Res. 48 (2020) e30, https://doi.org/10.1093/nar/gkaa017.
[45] J. Li, T. Deng, X. Chu, R. Yang, J. Jiang, G. Shen, R. Yu, Rolling circle amplification combined with gold nanoparticle aggregates for highly sensitive identification of single-nucleotide polymorphisms, Anal. Chem. 82 (2010) 2811–2816, https://doi.org/10.1021/ac100336n.
[46] B. Tian, J. Fock, G.A.S. Minero, F. Garbarino, M.F. Hansen, Ultrasensitive real-time rolling circle amplification detection enhanced by nicking-induced tandem-acting polymerases, Anal. Chem. 91 (2019) 10102–10109, https://doi.org/10.1021/acs.analchem.9b02073.
[47] B. Tian, J. Fock, G.A.S. Minero, M.F. Hansen, Nicking-assisted on-loop and off-loop enzymatic cascade amplification for optomagnetic detection of a highly conserved dengue virus sequence, Biosens. Bioelectron. 160 (2020), 112219, https://doi.org/10.1016/j.bios.2020.112219.
[48] A. Cao, C.Y. Zhang, Sensitive and label-free DNA methylation detection by ligation-mediated hyperbranched rolling circle amplification, Anal. Chem. 84 (2012) 6199–6205, https://doi.org/10.1021/ac301186j.
[49] J. Hu, M.H. Liu, C.Y. Zhang, Integration of isothermal amplification with quantum dot-based fluorescence resonance energy transfer for simultaneous detection of multiple microRNAs, Chem. Sci. 9 (2018) 4258–4267, https://doi.org/10.1039/c8sc00832a.
[50] B. Liu, J. Liu, Freezing directed construction of bio/nano interfaces: reagentless conjugation, denser spherical nucleic acids, and better nanoflares, J. Am. Chem. Soc. 139 (2017) 9471–9474, https://doi.org/10.1021/jacs.7b04885.
[51] K.L. Kelly, E. Coronado, L.L. Zhao, G.C. Schatz, The optical properties of metal nanoparticles: the influence of size, shape, and dielectric environment, J. Phys. Chem. B 107 (2003) 668–677, https://doi.org/10.1021/jp026731y.
[52] S.E. Skrabalak, L. Au, X. Li, Y. Xia, Facile synthesis of Ag nanocubes and Au nanocages, Nat. Protoc. 2 (2007) 2182–2190, https://doi.org/10.1038/nprot.2007.326.
[53] T. Fan, Y. Mao, Q. Sun, F. Liu, J.S. Lin, Y. Liu, J. Cui, Y. Jiang, Branched rolling circle amplification method for measuring serum circulating microRNA levels for early breast cancer detection, Cancer Sci. 109 (2018) 2897–2906, https://doi.org/10.1111/cas.13725.
[54] J. Kim, A.M. Yu, K.P. Kubelick, S.Y. Emelianov, Gold nanoparticles conjugated with DNA aptamer for photoacoustic detection of human matrix metalloproteinase-9, Photoacoustics 25 (2022), 100307, https://doi.org/10.1016/j.pacs.2021.100307.